ISSN 0015-4628, Fluid Dynamics, 2018, Vol. 53, No. 5, pp. 654–669. © Pleiades Publishing, Ltd., 2018.
Original Russian Text © T.R. Zakirov, A.A. Galeev, M.G. Khramchenkov, 2018, published in Izvestiya Rossiiskoi Akademii Nauk, Mekhanika Zhidkosti i Gaza, 2018, No. 5, pp. 76–91.

Pore-Scale Investigation of Two-Phase Flows in Three-Dimensional Digital Models of Natural Sandstones

T. R. Zakirov[1*], A. A. Galeev[1], and M. G. Khramchenkov[1,2***]**

[1] *Kazan Federal University, Institute of Geology and Petroleum Technologies, Kazan, Russia*

[2] *Federal State Institution "Federal Scientific Centre—Scientific Research Institute of Systems Development," Kazan, Russia*

Received November 1, 2017

Abstract—The results of numerical simulation of the processes of two-phase flow through a porous medium in three-dimensional digital models of the porous space of three natural sandstone samples are given. The calculations are carried out using the lattice Boltzmann equations and the digital field gradient model over a wide range of the capillary numbers and the viscosity ratios of injected and displaced fluids. The conditions of flow through a porous medium with capillary fingering, viscous fingering and with stable displacement front are revealed.

Key words: mathematical simulation, X-ray CT, heterogeneity of porous space, two-phase flows, capillary number, fingering, drainage.

DOI: 10.1134/S0015462818050087

The problems of two-phase fluid flows through porous media are topical in many branches of science and technics; among them we can note hydrogeology, pedology and soil sciences, underground water dynamics, and oil- and gas-field developments. Together with the gravity, the viscous, capillary, and inertia forces control two-phase fluid flow dynamics in the porous space. The paper by Lenormand et al. [1] is one of the first widely known experimental studies on the investigation of two-phase fluid flows in the pore-scale using artificially constructed two-dimensional models of porous media. In that investigation it was demonstrated that in the process of draining the distribution of two fluids in pores is controlled by two dimensionless parameters. These are the capillary number Ca defined as the ratio of the viscous and capillary forces and the viscosity ratio of non-wetting (injected) and wetting (displaced) phases M: $\mathrm{Ca} = \mu_{nw} u_{nw}/(\sigma \cos\theta)$ and $\mathrm{M} = \mu_{nw}/\mu_w$, where μ_w and μ_{nw} are the dynamic viscosities of the wetting and non-wetting phases, respectively, u_{nw} is the injection velocity of the non-wetting fluid, σ is the surface tension, and θ is the interfacial angle (wetting contact angle). In view of low velocities of flow through the porous medium and, respectively, low Reynolds numbers, the inertia forces are insignificant in the problems of this type.

In subsequent years, the authors of [2–7] identified three types of flows with reference to two-dimensional homogeneous and heterogeneous models, namely, these are flows with capillary fingering, viscous fingering, and with stable displacement front. The ranges of the parameters Ca and M were determined for each of the types of flow and the model of porous medium. The distinguishing features of the flow types were revealed on the basis of visual analysis of dynamics of the fluid distributions and it was also found that for intermediate values of Ca and M numbers both capillary and viscous fingerings are simultaneously formed in the sample (crossover zone [8]). The results of all these investigations contain the fundamental bases of two-dimensional flows on the pore scales; nevertheless, the structure of the porous space in these models is not natural. At present, it was carried out a few similar tests on the real three-dimensional samples, in particular, on the carbonate fractured types of porous media and the available results are given only in several studies of recent years [9–12].

The difficulty of the investigation of multiphase flow in 3D space consists in specifics of visualization and methods of nondestructive testing of the displacement of phase interface. One of the ways of "in

[*] E-mail: timurz0@mail.ru.
[**] E-mail: akhmet.galeev@mail.ru.
[***] E-mail: mkhramch@gmail.com.

situ" visualization of the fluid distribution in pores when carrying out the laboratory experiment on flow through porous medium was complemented using the fast synchrotron X-ray CT method with the time step of the order of 10 s [13, 14]. Such experiments are very expensive, require high-technology tools, and have limitations in the spatial-temporal resolution and the choice of the displacement parameters. Another way (see, e.g., [15, 16]) implies carrying out the computational filtration experiment using a high-resolution (at least 5 μm) digital model of the porous medium, obtained by means of the X-ray microtomography, which assigns to the real sample. This way makes it possible to carry out multivariant calculations over a wide range of the two-phase flow parameters.

The aim of our investigation is to study dynamics of two-phase flow of immiscible incompressible fluids using three-dimensional digital models of the porous space of natural sandstones with various seepage-capacity properties at various flow velocities, surface tensions, and phase viscosities over wide ranges of the parameters Ca and M. We intend to reveal the characteristic features of the flows with formation of capillary fingers, viscous fingers, and with the stable displacement front and estimate the displacement effectiveness in each of the flow regime on the basis of numerical description of the motion of the phase interface and three-dimensional visualization of fluid distribution dynamics.

1. MATERIALS AND METHODS OF INVESTIGATION

1.1. Justification of the Choice of Mathematical Model

By present time, the great experience on the investigation of multiphase flows in the calculation domains with an arbitrary arrangement of impermeable zones is accumulated. Two approaches are the most frequently encountered in the mathematical simulation of such processes. The first of them is based on solution of the Navier-Stokes equations with addition of source terms, which characterize the phase interaction, and the continuity equation. Depending on the method of description of the phenomena on the phase interface, the level set method [15], the volume-of-fluid method [16], and the phase-field model [17] can be distinguished. The above-mentioned methods acquired a reputation in simulation of two-phase flows including the digital models of porous media [18]. Nevertheless, these methods are characterized by both the labor-consuming numerical implementation and the long-time duration of calculations on large grids (greater than 1 million nodes).

The second approach is based on using the lattice Boltzmann method (LBM). As compared with the first approach, the LBM implies the simpler numerical implementation and the good adaptation ability in employing the parallel computing technologies and it acquired a reputation in solving the filtration problems [2, 3, 6, 9–11]. The Shan-Chen model [20], the color-gradient method [21], and the free-energy method [22] are the most widespread in the LBM for description of the phase interaction. As distinct from the color-gradient method, the Shan-Chen and free-energy models have numerical instability and can give incorrect results when the viscosity and density ratios for the considered fluids are greater than 10.

In the present study we have chosen the lattice Boltzmann equations and the color-gradient method as the most optimum methods for solving the formulated problems. Within the framework of the LBM the flow is considered from the viewpoint of dynamics of an particle ensemble with a given finite number of possible velocities. The flow domain is divided by a grid with cells, as a rule, of quadratic or cubic shape. The set of these cells composes the lattice. In time step Δt the particles can perform one act of transition between the neighboring lattice nodes without interaction one another. As the variables which describe the state of system at each of the grid nodes we use the one-particle distribution functions $f(\mathbf{r}, \mathbf{u}, t)$. This function shows the fraction of particles at an instant t located in the neighborhood of the end of a radius-vector $\mathbf{r}(x, y, z)$ in which the points have the coordinates from (x, y, z) to $(x + \Delta x, y + \Delta y, z + \Delta z)$ and the velocities vary over the range from $\mathbf{u}(u_x, u_y, u_z)$ to $\mathbf{u}(u_x + \Delta u_x, u_y + \Delta u_y, u_z + \Delta u_z)$ [19].

In the study we will consider the three-dimensional case. As the possible directions for displacement of the particle ensemble we will use the set D3Q19 which is specified as follows:

$$\mathbf{e}_1 = c \cdot (0,0,0), \quad \mathbf{e}_2 = c \cdot (1,0,0), \quad \mathbf{e}_3 = c \cdot (-1,0,0), \quad \mathbf{e}_4 = c \cdot (0,1,0), \quad \mathbf{e}_5 = c \cdot (0,-1,0),$$
$$\mathbf{e}_6 = c \cdot (0,0,1), \quad \mathbf{e}_7 = c \cdot (0,0,-1), \quad \mathbf{e}_8 = c \cdot (1,1,0), \quad \mathbf{e}_9 = c \cdot (-1,1,0), \quad \mathbf{e}_{10} = c \cdot (1,-1,0),$$
$$\mathbf{e}_{11} = c \cdot (-1,-1,0), \quad \mathbf{e}_{12} = c \cdot (1,0,1), \quad \mathbf{e}_{13} = c \cdot (-1,0,1), \quad \mathbf{e}_{14} = c \cdot (1,0,-1),$$

$$\mathbf{e}_{15} = c \cdot (-1, 0, -1), \quad \mathbf{e}_{16} = c \cdot (0, 1, 1), \quad \mathbf{e}_{17} = c \cdot (0, -1, 1),$$
$$\mathbf{e}_{18} = c \cdot (0, 1, -1), \quad \mathbf{e}_{19} = c \cdot (0, -1, -1),$$

where $c = \Delta l/\Delta t$ is the basic velocity (Δl is the grid step).

A distribution function $f_i(\mathbf{r}, t)$ is put in correspondence to each of the velocity vectors of this set $\mathbf{e}_i$ ($i = 1, \ldots, 19$).

The dynamics of the particle ensemble of each of the fluids can be described in several stages. The first stage is the streaming step. In this stage the particles are displaced to neighboring nodes in time Δt so that the directions of the particle velocities do not change. In the second stage the process of particle collisions is considered ("collision step"). As a result of this stage, the particle distribution function tends to the equilibrium state. In the third stage the interaction between the fluids on the interface, as well as the interaction with the solid phase, is described. The time and space evolution of the distribution functions of each of the fluids is described by the equation

$$f_i^k(r + \mathbf{e}_i\Delta t, t + \Delta t) = f_i^k(\mathbf{r}, t) + (\Omega_i^k(\mathbf{r}, t))^1 + (\Omega_i^k(\mathbf{r}, t))^2, \tag{1.1}$$

where $k = 1,\ 2$ denotes the type of the liquid, i.e., the wetting and non-wetting phases, respectively.

Depending on the form of the collision operator $(\Omega_i^k)^1$ in Eq. (1.1), two models, namely, the single relaxation time model (SRT-model) [23] and the multi relaxation time model (MRT-model) [24], are distinguished. From comparison with the analytical solutions it follows that the accuracy of the results obtained using the MRT-model is significantly higher than that of SRT-model [23]; therefore, in the present study we use the MRT-model.

The relaxation parameter τ^k is crucial in the LBM. It controls the kinematic viscosity μ^k and is connected with it by the following relation:

$$\mu^k = \left(\frac{2\tau^k - 1}{6}\right)\frac{\Delta l^2}{\Delta t}.$$

In the LBM the equations are solved in the "density–velocity" variables. The macroscopic density and velocity components of each of the fluids in cells are calculated from the formulas

$$\rho^k(\mathbf{r}, t) = \sum_{i=1}^{19} f_i^k(\mathbf{r}, t),$$
$$\mathbf{u}^k(\mathbf{r}, t) = \frac{1}{\rho^k}\sum_{i=1}^{19} \mathbf{e}_i f_i^k(\mathbf{r}, t).$$

In the LBM the pressure p^k created by each of the fluids is connected with its density by the following relation: $p^k = \rho^k c^2/3$ [19].

For describing the phenomena on the interfaces between the fluids and the fluids and the solid surfaces, in the present study we use the color-gradient method [21]. It consists of three stages. The first stage represents calculations of the gradient of the color field $\mathbf{g}$ whose components are calculated from the formula

$$\mathbf{g}(\mathbf{r}, t) = \sum_{i=1}^{19} \mathbf{e}_i \left(f_i^2(r + \mathbf{e}_i\Delta t, t) - f_i^1(r + \mathbf{e}_i\Delta t, t)\right).$$

Traditionally, red color is put in correspondence to one of the fluids and blue color to the other. On the interface between two liquids and the solid phase the wetting contact angles (interfacial angles) are specified by means of assigning values of the density to the cells related to the skeleton of the porous medium. In the second stage it is assumed to describe the effects of surface tension on the interface between the liquids and between the liquids and the rigid surfaces as follows:

$$(\Omega_i^k)^2 = \frac{A}{2}|\mathbf{g}|\left(2\cos^2(\alpha_i) - 1\right),$$

where A is the parameter which controls the surface tension and α_i is the angle between the vector $\mathbf{g}$ and the direction of $\mathbf{e}_i$. The third stage is the modification of the function f_i^k after solving Eq. (1.1) with regard to the operators $(\Omega_i^k)^1$ and $(\Omega_i^k)^2$:

$$(f_i^2)^* = \frac{\rho^2}{\rho} f_i + \beta \frac{\rho^1 \cdot \rho^2}{\rho} f_i^{eq} \cos(\alpha_i), \tag{1.2}$$

$$(f_i^1)^* = \frac{\rho^1}{\rho} f_i - \beta \frac{\rho^1 \cdot \rho^2}{\rho} f_i^{eq} \cos(\alpha_i), \tag{1.3}$$

where $\rho = \rho^2 + \rho^1$, $f_i = f_i^1 + f_i^2$, and f_i^{eq} is the equilibrium distribution function [19, 23] calculated for the density ρ and zero velocity

$$f_i^{eq}(\rho, \mathbf{u}) = w_i \rho(r) \cdot \left(1 + 3\frac{(\mathbf{e}_i \cdot \mathbf{u})}{c^2} + 4.5\frac{(\mathbf{e}_i \cdot \mathbf{u})^2}{c^4} - 1.5\frac{\mathbf{u}^2}{c^2}\right).$$

The weight coefficients are equal to $w_1 = 1/3$, $w_{2-8} = 1/18$, and $w_{9-19} = 1/36$. These numerical values of the weight coefficients are due to the fact that, since $f_i(\mathbf{r}, t)$ is the probability characteristic, then the condition $\sum\limits_{i=1}^{n} w_i = 1$, where n is the number of possible directions, must be satisfied for any set of possible directions (for example, D2Q9, D3Q15, D3Q17, or D3Q27).

In Eqs. (1.2) and (1.3) the parameter β controls the thickness of the interface between the liquids. In the present study its value is equal to 0.8 and cannot be greater than unity.

As the boundary conditions on the rigid inner and outer impermeable boundaries of the flow region, we use the "bounce back" conditions [19] which are analogs of the no-flow and no-slip conditions for liquid in the classical hydrodynamic formulation of the problem. The fluid pressure and the velocity components normal to the boundary (equal to zero) are assumed to be known on the inlet and outlet boundaries. In the LBM such conditions are specified using the Zou and He relations [25].

The mathematical model described above was implemented numerically on the Intel Fortran programming language in the Visual Studio 2010. The calculations were carried out on a computing station containing two Intel Xeon processors, each of them has 20 logic cores, with the use of the OpenMP parallel computation technology. The calibration of the numerical parameters controlling the phase interface thickness, the surface tension, and the angles of wetting with respect to the theoretical values of these quantities is given in [21, 26].

The numerical results obtained on the basis of the program code were compared with the known analytical solutions and results of other authors. As the first example, we have considered the problem of laminar stratified flow of two immiscible liquids in a cylindrical pipe for various relations of the viscosities μ_1 and μ_2 in the absence of the effects of wetting and interphase tension. In this formulation, the streamwise velocity components of each of the fluids can be described by the following analytical dependences [26]:

$$u_x^1(y) = \frac{\Delta P \cdot r^2}{2\mu_1 L}\left(-\left(\frac{y}{r}\right)^2 + \frac{y}{h}\left(\frac{\mu_1 - \mu_2}{\mu_1 + \mu_2}\right) + \frac{2\mu_1}{\mu_1 + \mu_2}\right), \quad -r \le y \le 0, \tag{1.4}$$

$$u_x^2(y) = \frac{\Delta P \cdot r^2}{2\mu_2 L}\left(-\left(\frac{y}{r}\right)^2 + \frac{y}{h}\left(\frac{\mu_1 - \mu_2}{\mu_1 + \mu_2}\right) + \frac{2\mu_2}{\mu_1 + \mu_2}\right), \quad 0 \le y \le r. \tag{1.5}$$

In Eqs. (1.4) and (1.5) the coordinate y is perpendicular to the flow direction, $\Delta P = 10$ Pa is the pressure difference between the inlet and outlet boundaries, $r = 125$ μm is the pipe radius, $L = 372.5$ μm is the pipe length, $\mu_2 = 1$ mPa s, and $\mu_1 = 2$, 10, and 25 mPa s. In Fig. 1 we have compared the numerical and analytical solutions. The mean relative deviation of the numerical calculations from the analytical dependence is not greater than 0.4%.

As the second example, we have considered the problem of displacement of a wetting phase from a cylindrical pipe, saturated with the wetting phase at the initial instant of time, by injecting a non-wetting liquid. The calculation results were compared with the numerical solutions of the identical problem considered in [27]. The grid dimension was 200×20 nodes, the grid step was equal to 3 μm, $\sigma = 20$ mN/m, $\theta = 60^\circ$, and $\Delta P = 1500$ Pa. At the initial instant of time the region $0 < x < 0.05L$,

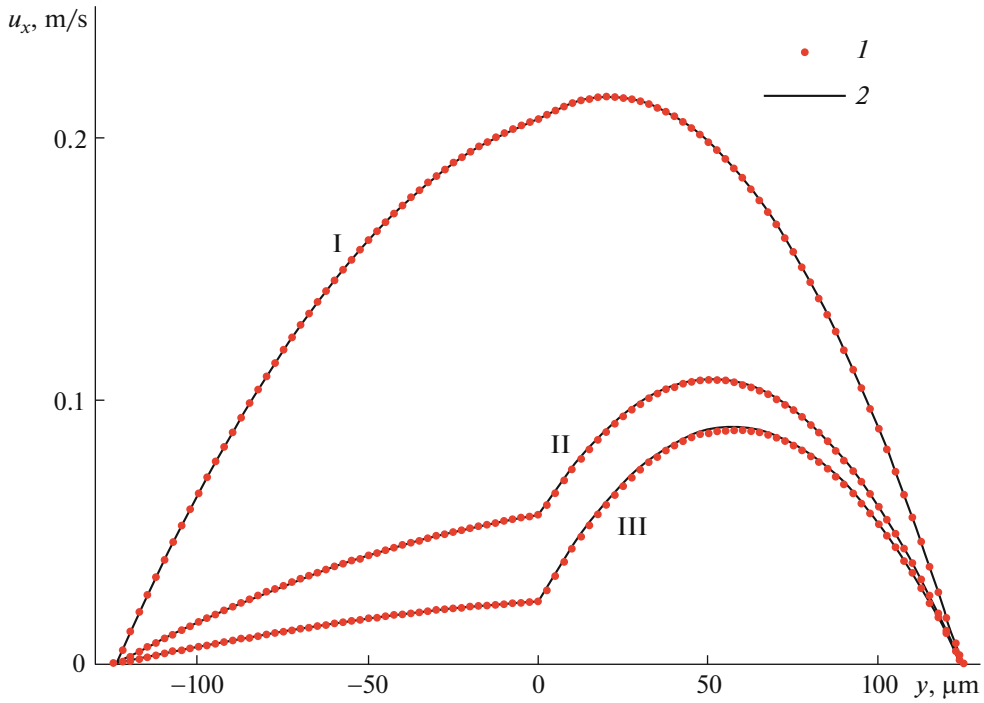

Fig. 1. Distribution of the streamwise velocity component of stratified flow of two immiscible liquids in the cylindrical channel. Comparison of the analytical and numerical solutions: curves *1* and *2* correspond to the numerical and analytical solutions, respectively; $\mu_1/\mu_2 = 2/1$ (I), $\mu_1/\mu_2 = 10/1$ (II), and $\mu_1/\mu_2 = 25/1$ (III).

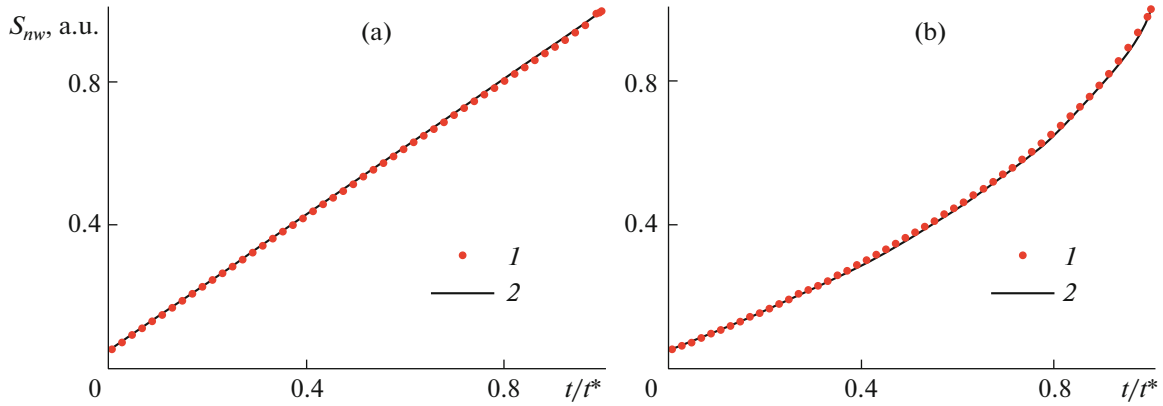

Fig. 2. Time variation in the saturation of the cylindrical pipe with the non-wetting phase S_{nw}: M= 1 (a) and $M = 0.1$ (b); curves *1* and *2* correspond to the numerical and analytical solutions, respectively (borrowed from [27]).

where L is the pipe length, was occupied by the non-wetting phase. The problem was solved for $M = 1$ and 0.1. In Fig. 2 we have compared the calculation results. In accordance with Fig. 2, the agreement of the results can be taken to be satisfactory. In this figure t is the current instant of time and t^* characterizes the instant of time at which the flow region does not contains any wetting liquid at all.

1.2. Samples of Investigation

As the samples nos. 1–3 of porous media, we used oil-saturated sandstones with various filtration-capacity properties taken from the Bobrikov horizon (depth of 1535.2–1535.4 m) of the Eastern-Birlin oil-field located in the Ul'yanovsk region. The X-ray microtomographic scannings of the sample nos. 1 and 3 with resolution of 3.2 μm and the sample no. 2 with resolution of 1.5 μm were carried out to construct the 3D digital models. In Figs. 3a–3c we have reproduced the digital model of the sample

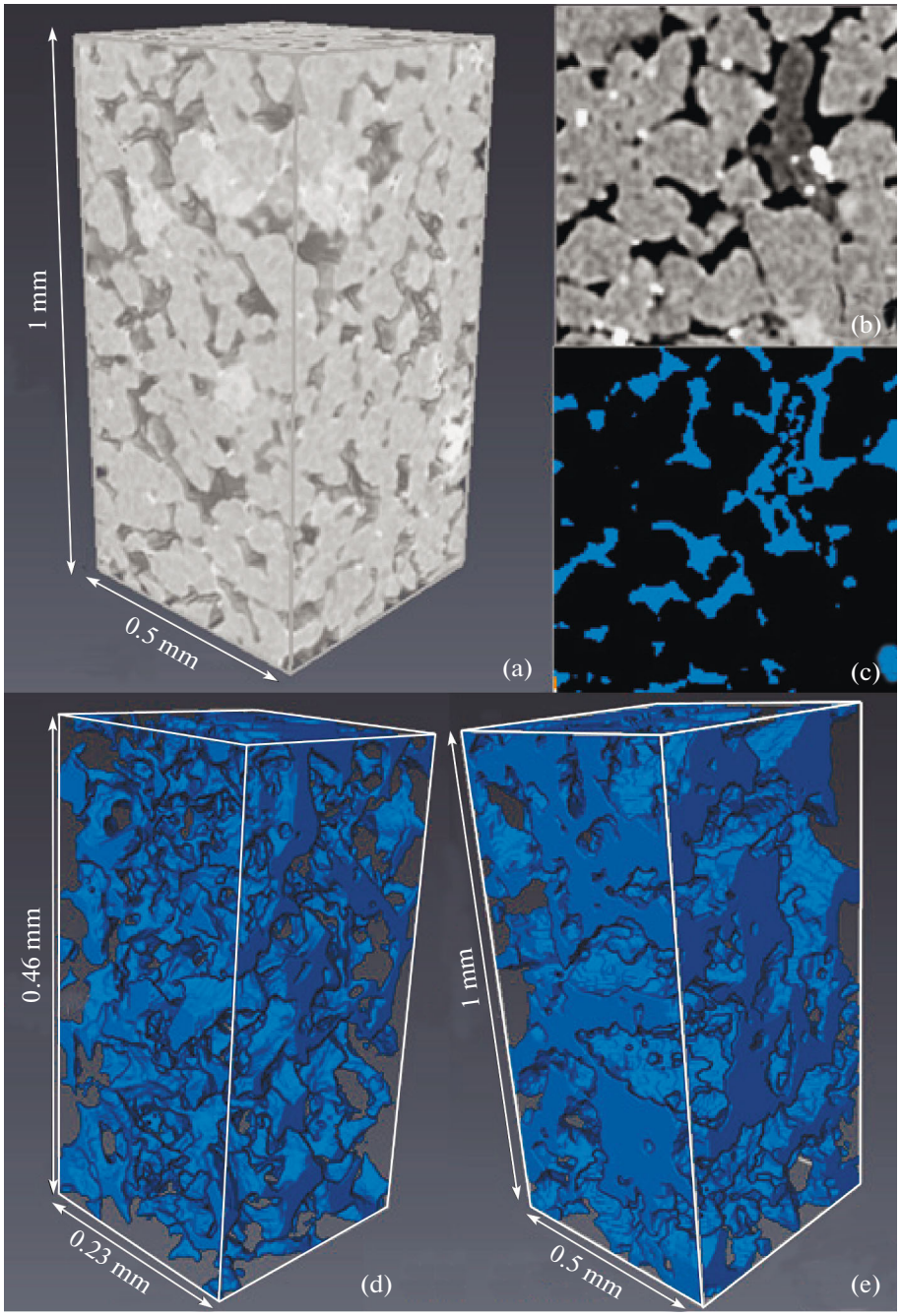

Fig. 3. Digital microtomographic models: 3D model of the sample no. 1 (a); slice of the sample no. 1 in the XY plane (b); the same slice after binarization, the dark blue and black colors correspond to the pore and the skeleton, respectively (c); porous space of the sample no. 2 (d); porous space of the sample no. 3 (e).

no. 1. In Figs. 3a and 3b the grey shades characterize the intensity of X-ray attenuation by various sections of the sample, namely, the light-gray shades correspond to the sandstone granules and the black tones to the porous space. To construct the digital model of the computing grid the image was binarized, i.e., it was divided into cells which belong to either the porous space or the skeleton (Fig. 3c). The images were processed using the AVIZO Fire programm (Visualization Sciences Group). The methods and types of the image segmentations were described in [28]. In Figs. 3d and 3e we have reproduced the structure of the porous space of the sample nos. 2 and 3, respectively.

Table 1.

No. of the sample	Porosity, rel. units	Principal components of the permeability tensor			Size distribution of the open pores	
		$k_{XX}, \mu\text{m}^2$	$k_{YY}, \mu\text{m}^2$	$k_{ZZ}, \mu\text{m}^2$	mean pore diameter in μm	root-mean-square deviation in μm
1	0.217	0.523	0.607	0.553	16.1	6.5
2	0.239	0.194	0.195	0.241	4.2	1.5
3	0.221	1.33	1.395	1.084	20.8	8.1

1.3. Formulation of the Computational Experiments

At the initial instant of time the porous space is entirely occupied by the liquid wetting the skeleton. In the calculations the angle of wetting was equal to 0°. The injected phase is supplied to the conventionally left-hand face of the sample, which is perpendicular to the OX axis, with a given constant flow velocity in each of the cells; the fluids flow out across the conventionally right-hand face of the sample, which is perpendicular to the OX axis, on which the pressure is maintained constant in the course of the experiment. The remaining four external faces of the computation domain are assumed to be impermeable. The calculations were carried out over a wide flow velocity range: $(0.1, 0.15, 0.25, 0.35, 0.5, 0.75, 1.0, 1.5, 2.0, 3.0, 4.0) \times 10^{-3}$ m/s; $\sigma = 2$, 20, and 40 mN/m (the last value is used only in a single variant of the calculations to decrease Ca when $M = 0.1$); the viscosity of the phases are 1 and 10 mPa s so that $M = 0.1$, 1, and 10. For these parameters Ca varies over the range from -5.6 to -1.7.

The choice of dimensions of a sample is based on the representativeness of its filtration characteristics (so-called representative elementary volume or REV), at least, on the lab-scale (tens of millimeters). According to the methods described in [29, 30], it was revealed that the digital image of the model of cubic shape, used in the present study, of dimension more than 200 cells (or greater than 0.6 mm) is representative for measuring the porosity coefficients and the component of the absolute permeability k_{XX}. However, the estimations of the REV for two-phase flow characteristics carried out in [31] with the use of the Fontainebleau sandstone (Basin Parisienne, France), that is standard for testing, showed that the topically small samples of 2–3 mm dimensions used in the X-ray tomography scanning are not representative. For this reason, in view of the large calculation volume, the verification of representativeness of the samples tested in the present study for the two-phase flow characteristics was not carried out. Nevertheless, this fact is not the obstacle for revealing the features inherent in various types of flows, while the question of rescaling the multiphase flows requires an individual consideration. The restriction on the model dimension is also due to adequacy of the time expenditures on the calculations. The grids of the input binarized digital core samples contain about 800×10^6 cells from which the fragments of dimensions of $300 \times 150 \times 150$ cells were cut. In Table 1 we have presented the filtration-capacity properties of the digital samples.

The distribution of the permeable (or open) pores over the cross-section diameters was estimated on the basis of the capillary pressure drainage curves using the Laplace formula.

2. RESULTS AND DISCUSSIONS. CLASSIFICATION OF THE FLOW PATTERNS

Figure 4 illustrates the non-wetting phase distribution patterns in the porous channels of the sample no. 1 at the instant of its breaking through the output cross-section for $\text{Ca} = 2 \times 10^{-3}$ (Fig. 4a), 2.5×10^{-5} (Fig. 4b), 1.2×10^{-5} (Fig. 4c), and 2.5×10^{-6} (Fig. 4d) when $\text{M} = 0.1$. We can clearly see that the regime of the filtration experiment affects significantly the fluid distribution structure in the pores. Different values of Ca correspond to different systems of porous channels saturated by the injected phase. Moreover, even a relatively small change in the value of the parameter Ca from 2.5×10^{-5} to 1.2×10^{-5} (Figs. 4b and 4c) leads to a considerable flow redistribution in the sample. As distinct from the two-dimensional images, frequently, in the case of three-dimensional images it is fairly difficult to analyze visually the displacement of fluid in pores. In the present study, the two-phase flow dynamics

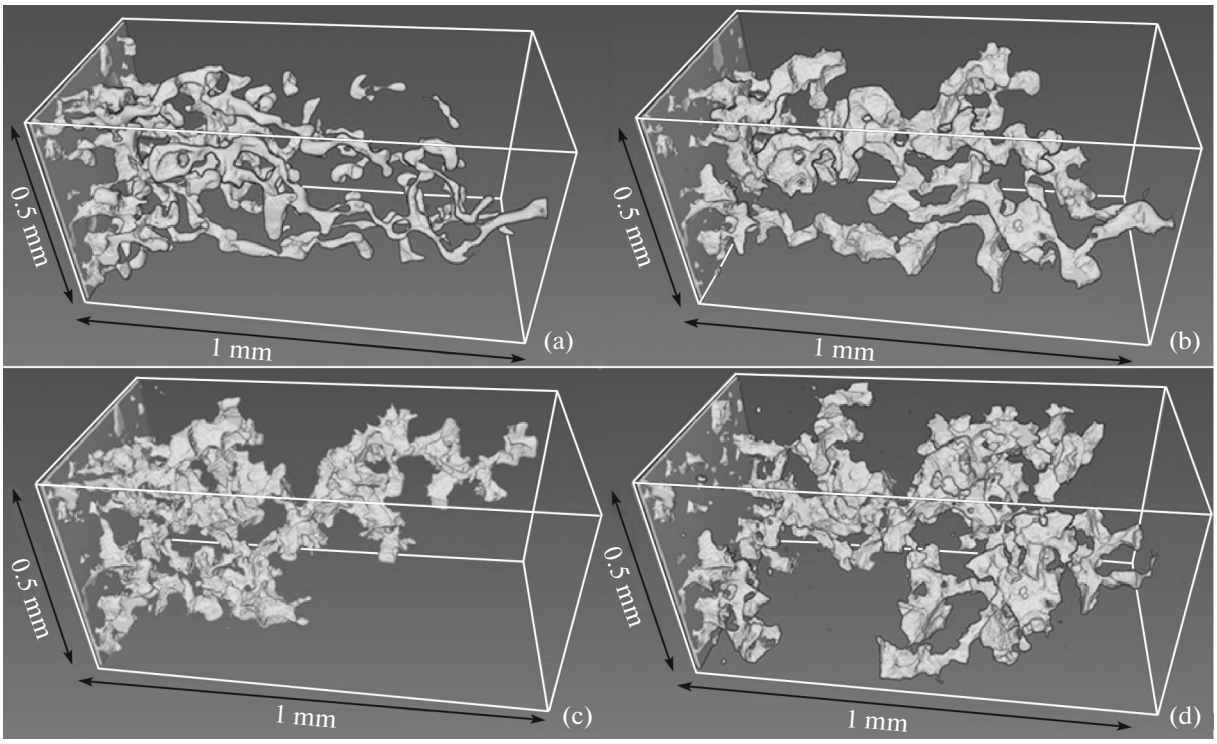

Fig. 4. Distribution of the non-wetting phase in the porous space of the sample no. 1 at the instant of its breaking through the output cross-section for various displacement parameters; flows: with viscous fingering (a); in the crossover regime (b, c); with capillary fingering (d); $\log_{10}\mathrm{Ca} = -2.7$ (a), -4.6 (b), -4.9 (c), -5.6 (d); $\log_{10}\mathrm{M} = -1$ (a–d).

are proposed to describe numerically in the form of the graph of the saturation of a sample by the non-wetting liquid as a function of the cell coordinate along the OX axis, where the phase interface is located, which is nearest to the output cross-section or the leading front (Fig. 5).

2.1. Flows in the Capillary Fingering Regime

We will consider the displacement regimes which correspond to the values of the parameters Ca and M in Fig. 5a with low flow velocities and high surface tensions (corresponding to given regimes for each of the samples). In Fig. 6 we have shown the Ca and M numbers. For the given parameters the capillary forces predominate the viscous forces and are crucial for displacement of the phase interface in the porous space. The given fluid flow rate is maintained by the pressure difference between the inlet and outlet faces of the sample, the displacement being occurred through the channels which ensure its minimum value for the current fluid distribution. In this regime the pores with the maximum transverse cross-sections are priority for the motion of the phase interface.

The dynamics of the phase interface displacement in the porous space characteristic of such a force relation, shown in Figs. 5a and 7 for the sample no. 1 in the case of $\log_{10}\mathrm{Ca} = -5.6$ and $\log_{10}\mathrm{M} = -1$, have a series of distinctive features. From Figs. 7a–7e we can see that the coordinate of the leading front along the OX axis did not vary in the current time interval and is equal to 206 cells. In analyzing the fluid distributions corresponding to Figs. 7a–7c, we estimated the dimensions of channels in which the leading front is localized and the phase interface is moving. It is found that the front stopped in the pore with the cross-sectional dimension of approximately 10 μm (Fig. 7a), while the front continues to move through two wider channels, namely, of the cross-sectional dimensions 18 and 15 μm (these regions are distinguished in Figs. 7b and 7,c by the white frames). In accordance with Fig. 5a, the events of stopping the leading front in the course of the computational experiments occur repeatedly and its movement in the direction to the output cross-section is stepwise. During the time while the coordinate of the leading front is steady, the wetting phase continues to be displaced behind the front (Figs. 7b–7e). Partially owing to such a mechanism, the effectiveness of the porous space filling by the non-wetting

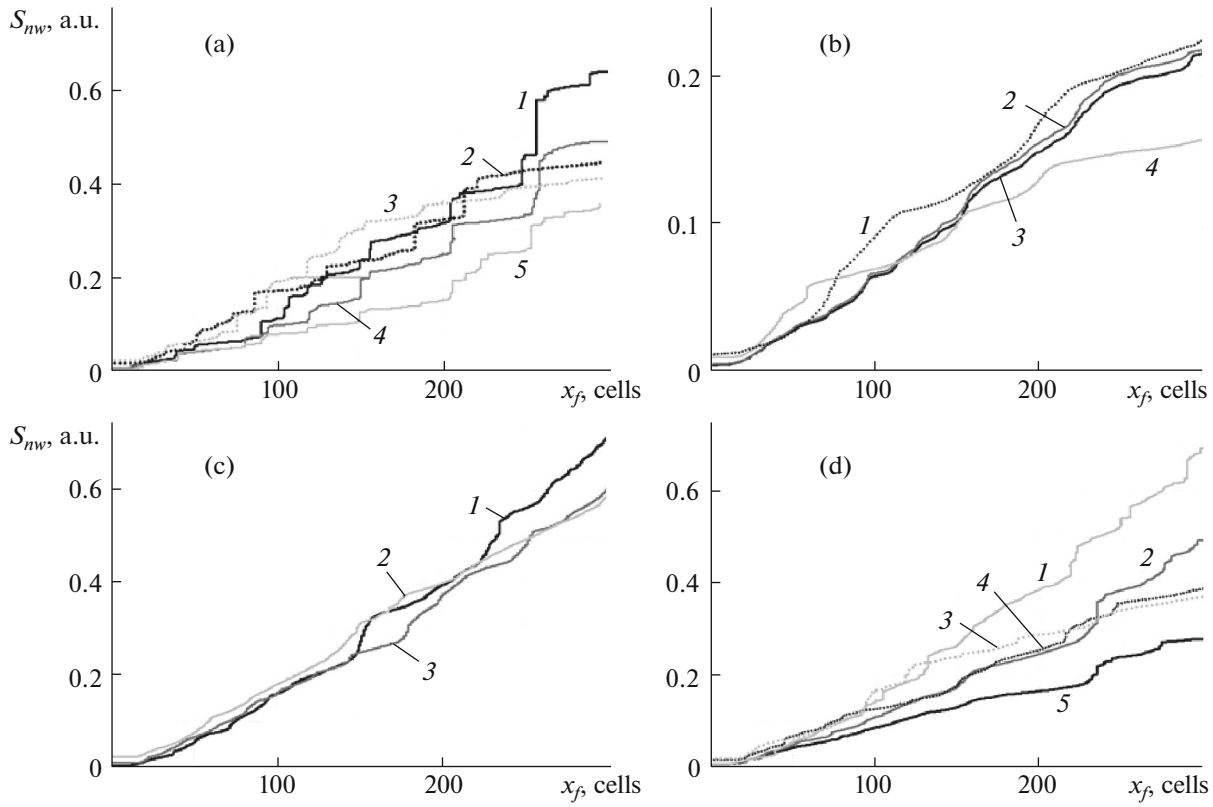

Fig. 5. Saturation of a sample by the non-wetting phase S_{nw} as a function of the coordinate of the leading front x_f along the OX axis, constructed for samples of flows with capillary fingering (a), with viscous fingering (b), with the stable displacement front (c), and in the crossover zone (d): the sample no. 1 (curves *1, 4,* and *5*), the sample nos. 2 and 3 (curves *2* and *3*); $\log_{10}$ Ca = −4.3, −3.9, −4.3, −4.6, and −5.6 (curves *1*–*5*, respectively); $\log_{10}$ M = 1 (curves *1* and *3*), 0 (curves *2* and *4*), −1 (curve *5*) (a); the sample no. 1 (curves *2* and *3*), no. 2 (curve *4*), and no. 1 (curve *3*); $\log_{10}$ Ca = −2.7 (curves *1* and *3*), −3 (curve *2*), and −3.3 (curve *4*); $\log_{10}$ M = −1 (curves *1*–*4*) (b); the sample no. 1 (curve *1*), no. 2 (curve *3*), and no. 3 (curve *2*); $\log_{10}$ Ca = −2, −2.3, and −1.7 (curves *1*–*3*, respectively); $\log_{10}$ M = −1 (curves *1*–*3*) (c); and the sample no. 1 (curves *1* and *5*), no. 3 (curves *2* and *3*), and no. 2 (curve *4*); $\log_{10}$ Ca = −3.6 (curve *1*), −3.3 (curves *2* and *4*), −4 (curve *3*), and −4.6 (curve *5*); $\log_{10}$ M = 1 (curves *1* and *2*), 0 (curves *3* and *4*), and −1 (curve *5*) (d).

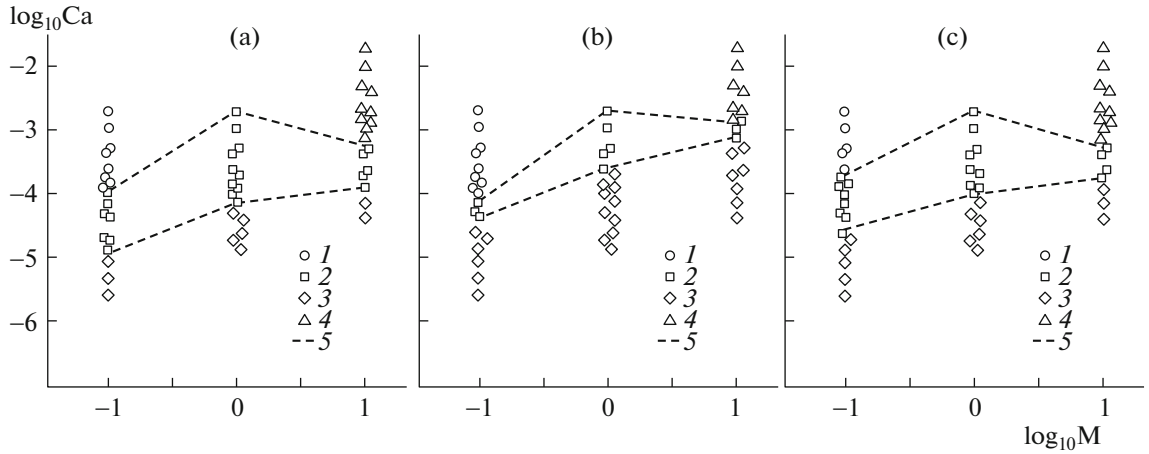

Fig. 6. Phase diagrams of the flow regimes in the coordinates $\log_{10}$ M– $\log_{10}$ Ca: the samples no. 1 (a), no. 2 (b), and no. 3 (c); symbols *1*–*4* correspond to viscous fingering, crossover, capillary fingering, and stable displacement, respectively; and lines *5* correspond to the boundaries of the flow regimes.

fluid, as compared with the viscous fingering regime (Fig. 5b), is significantly higher. The distinctive feature of flows with formation of capillary fingers shown in Fig. 7 is their development non only in the direction of the created pressure difference along the OX axis, but also in different directions, including opposite directions. The coordinate of the leading front is displaced in the time interval between the images reproduced in Figs. 7e and 7f. In analyzing Fig. 7f, we have revealed that the location of the phase interface, which is the leading front in Figs. 7a–7e in the previous instants of time, remains the

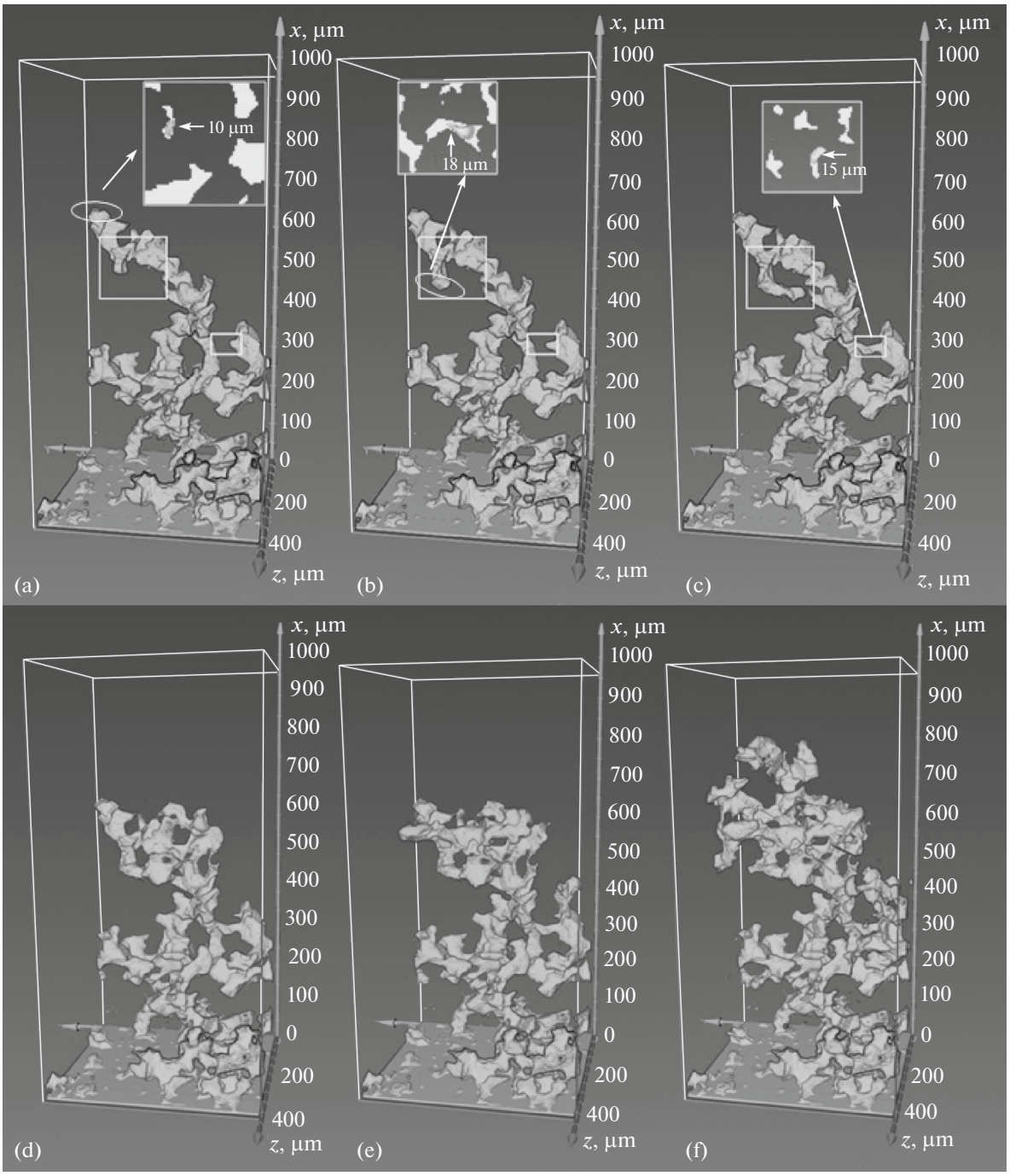

Fig. 7. Dynamics of the non-wetting fluid distribution in the porous space of the sample no. 1 in the capillary fingering regime: $\log_{10} \mathrm{Ca} = -5.6$ and $\log_{10} \mathrm{M} = -1$; (a, b) show the slices in which the phase interfaces are localized; (c) show the slice in which there is a porous channel occupied by the non-wetting fluid and its thickness is given; (d, e) show the displacement of the wetting fluid behind the leading front; and (f) shows the movement of the leading front through a new system of porous channels.

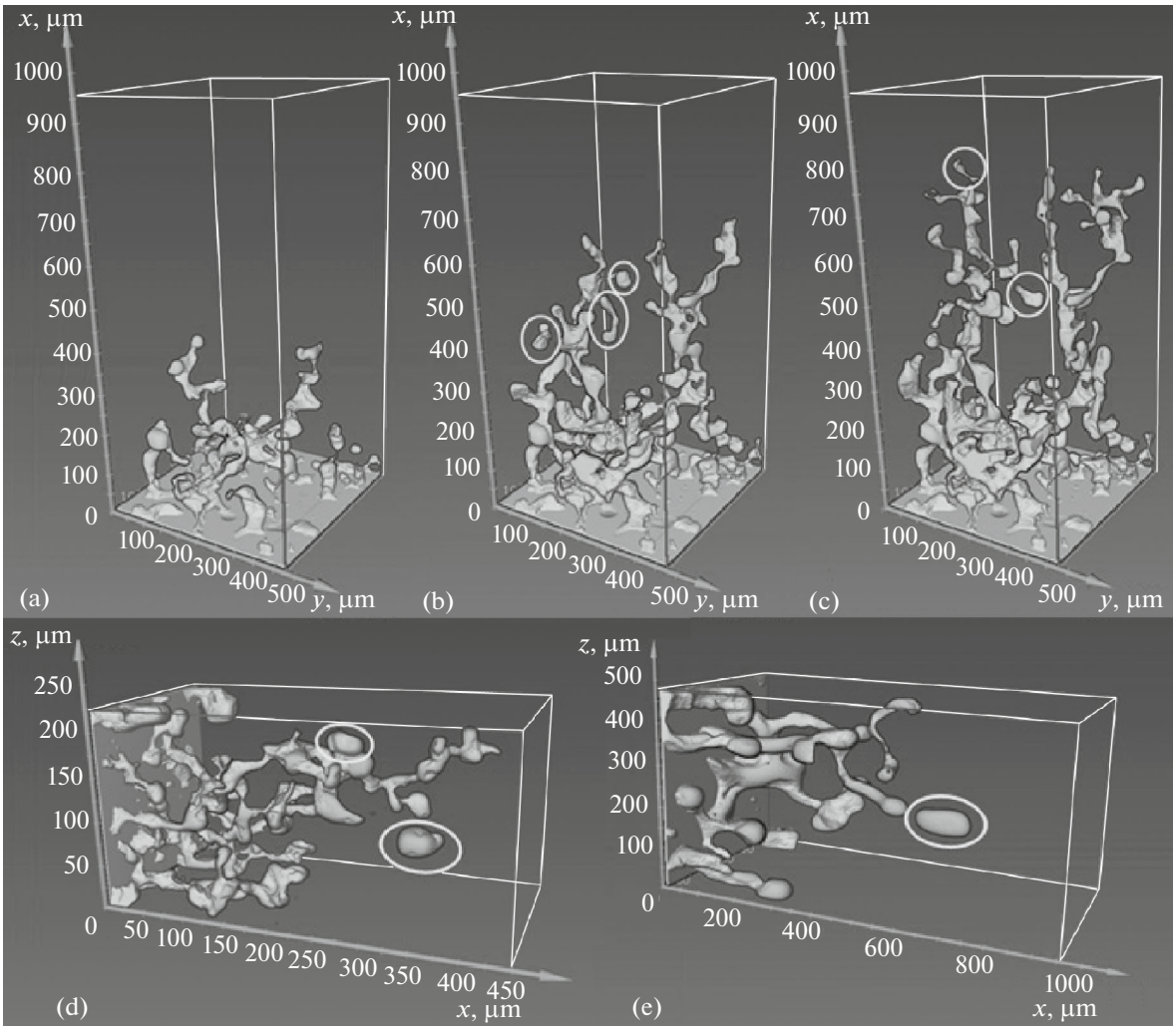

Fig. 8. Non-wetting fluid distribution over the porous space in the viscous fingering regime: sample no. 1, $\log_{10}\mathrm{Ca} = -3.0$, and $\log_{10}\mathrm{M} = -1$ (a–c); sample no. 2, $\log_{10}\mathrm{Ca} = -2.7$, and $\log_{10}\mathrm{M} = -1$ (d); and sample no. 3, $\log_{10}\mathrm{Ca} = -2.7$, and $\log_{10}\mathrm{M} = -1$ (e); the separate volumes of the non-wetting phase are shown in round frames.

same. Respectively, the movement of the new leading front in the direction toward the outlet cross-section occurs already through another system of porous channels. Similar flow specifics for which the following features are characteristic: stepwise motion of the leading front, formation of capillary fingers in the directions different from the direction of the created pressure difference, episodes of stopping the front, and priority of channels of the wider cross-section for movement of the interphase front,—is also observed for the samples nos. 2 and 3 (Fig. 5a) which have other filtration-capacity properties.

2.2. Flows in the Viscous Fingering Regime

At present, the problem of instability of the interphase front is frequently investigated with reference to the Hele–Shaw cell [32]. In accordance with the investigations, viscous fingering develops only when $\mathrm{M} < 1$ at low capillary resistances. Relying on these regularities, in this section we will consider flows at high velocities and low surface tensions. In Fig. 6 we have shown the Ca numbers corresponding to given regimes for each of the samples. In Fig. 5b we have reproduced the growth of viscous fingering and the dynamics of the leading front: for the sample no. 1 when $\log_{10}\mathrm{Ca} = -3.0$ and $\log_{10}\mathrm{M} = -1$ (Figs. 8a–8c); for the sample no. 2 when $\log_{10}\mathrm{Ca} = -2.7$ and $\log_{10}\mathrm{M} = -1$ (Fig. 8d); and for sample no. 3 when $\log_{10}\mathrm{Ca} = -2.7$ and $\log_{10}\mathrm{M} = -1$ (Fig. 8e). In analyzing the images in Fig. 8, for all three samples we revealed that in the neighborhood of the inlet boundary the majority of the porous channels of various cross-sections, as distinct from the capillary fingering regime (Fig. 7), are occupied

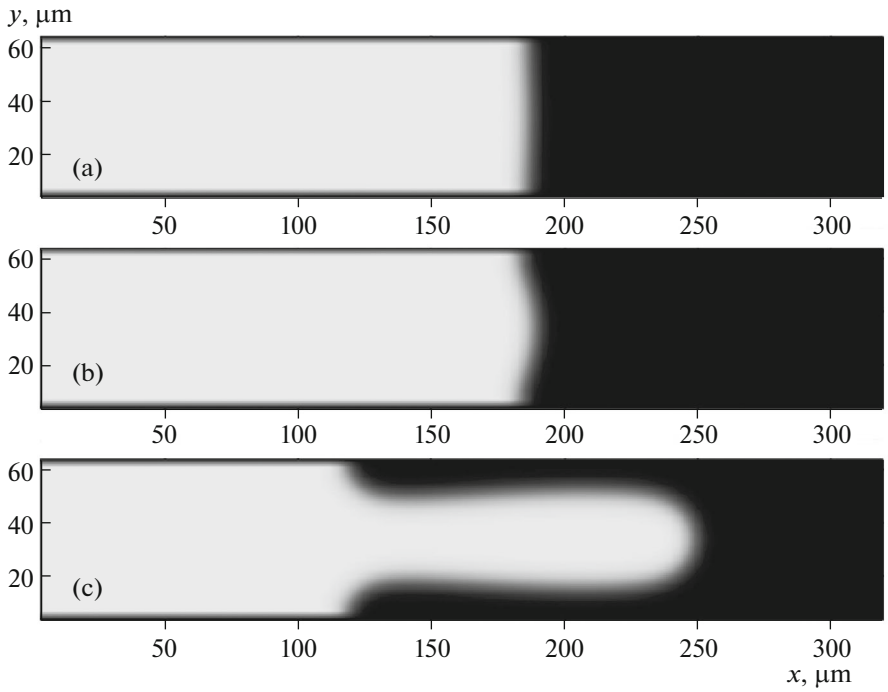

Fig. 9. Distribution of two liquids in their combined flow in the cylindrical channel; the white and black colors correspond to the non-wetting and wetting phases, respectively. The flow parameters: $u_{nw} = 0.01$ m/s and $\sigma = 0.2$ mN/m (a); $u_{nw} = 0.05$ m/s and $\sigma = 0.2$ mN/m (b); and $u_{nw} = 0.1$ m/s and $\sigma = 0.2$ mN/m (c).

by the injected fluid. The formation of viscous fingers is owing to different velocities of the movement of the interphase front in pores due to heterogeneity of the porous space structure. As can be seen in Fig. 8, in each of the samples there are several filtration channels with the higher velocity of the non-wetting phase. In such pores the regions occupied by the injected fluid are viscous fingers. As distinct from the capillary fingering regime, the viscous fingers are predominantly formed in the direction to the outlet cross-section. Since the displacement is especially expressed only in a small volume of the porous space, then the effectiveness of its filling with the non-wetting phase is low. According to Fig. 5b, it is only 15–25% at the instant of breakthrough. No episodes of stopping the front and deviations of streams in opposite direction are observed. The monotonic character of the curves in Fig. 5b testifies this fact. In view of the weak interphase tension and high velocities, the formation of isolated volumes of injected fluid (in Fig. 8 they are distinguished by round frames) with various geometric shapes is characteristic of this type of flow. This phenomenon is the indication of formation of emulsions.

A comparison of Figs. 7 and 8 makes it possible to note that the viscous fingers are thinner as compared with the capillary fingers. To explain this phenomenon we carried out a series of calculations of displacement of the wetting liquid from the cylindrical pipe of dimensions 100×20 cells with the grid step of 3.2 μm at various velocities and constant interphase tensions ($M = 0.1$ in all the variants). In Fig. 9 we have reproduced the fluid distributions at the saturation by injected fluid of 52%. In accordance with these distributions, an increase in the flow velocity leads to an increase in the area of the phase interface and formation of a viscous finger (Fig. 9c) elongated toward the outlet cross-section. In this case a significant part of the wetting liquid is localized between the pipe walls and the interface between two phases. This can partially explain the low effectiveness of displacement in these regimes.

2.3. Flows with Stable Displacement Front

As in Section 2.2, we will consider flows at high velocities and low capillary resistances but for $M = 10$. In Fig. 6 we have shown the Ca numbers corresponding to given regimes. In each of the samples the velocity of the leading front is close to constant (linear nature of the curves in Fig. 5c); however, as distinct from the viscous fingering regime, more than 59% of the wetting liquid are displaced from the porous space. In Fig. 10 we have plotted the non-wetting fluid distributions over the transverse

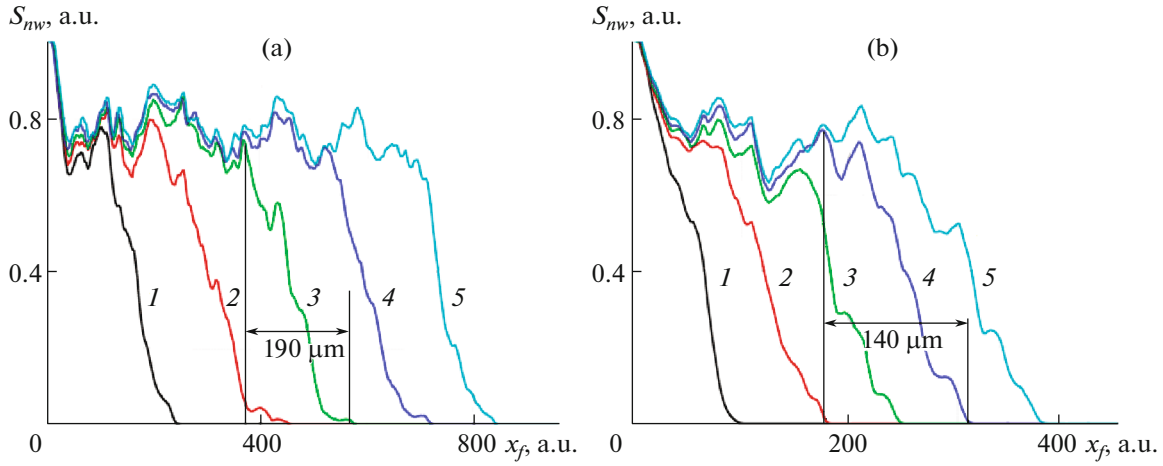

Fig. 10. Saturation of a sample by the non-wetting phase S_{nw} as a function of the distance from the inlet cross-section x_f at various instants of time: the sample no. 1, $\log_{10}\mathrm{Ca} = -2.0$, and $\log_{10}\mathrm{M} = 1$ (a) and the sample no. 2, $\log_{10}\mathrm{Ca} = -2.3$, and $\log_{10}\mathrm{M} = 1$ (b); curves *1*–*5* correspond to $1 \times 10^5\Delta t, 2 \times 10^5\Delta t, 3 \times 10^5\Delta t, 4 \times 10^5\Delta t$, and $5 \times 10^5\Delta t$, respectively.

cross-sections of a sample at various instants of time: (a) for the sample no. 1 ($\log_{10}\mathrm{Ca} = -2.0$ and $\log_{10}\mathrm{M} = 1$) and (b) for the sample no. 2 ($\log_{10}\mathrm{Ca} = -2.3$ and $\log_{10}\mathrm{M} = 1$). We will compare two curves for the sample nos. 1 and 2, for example, at $t = 3 \times 10^5\Delta t$ and $4 \times 10^5\Delta t$. On the first curves we can distinguish cross-sections behind which the displacement is weakly expressed and the saturation by injected fluid is greater than 65–70% (in Fig. 10 such cross-sections are distinguished by vertical lines). Consequently, almost all the set of mobile phase interfaces is located in the zone ahead of such a cross-section and their collection forms the displacement front which is "smeared out" lengthwise and amounts to 190 and 140 μm for the first and second samples, respectively. The same flow pattern can be also observed for the sample no. 3 for which the front thickness amounts to 210 μm. It should be noted that in the case of homogeneous porous media in the stable displacement regime the interphase front is the plane surface perpendicular to the direction of motion, while in the heterogeneous medium the front can be considered to be plane quite relatively.

2.4. Flows in the Crossover Zone

In the case of intermediate values of Ca (Figs. 5d and 6) the viscous friction and capillary resistance forces are commensurable quantities. In such regimes both capillary and viscous fingers are simultaneously formed in the sample (Figs. 4b and 4c). As in the two-dimensional models (Fig. 5d), it is difficult to reveal the features of combined displacement characteristic of given parameters. Such flows can be observed in each of the samples, they develop for all the M numbers and form the transition crossover zone.

3. PHASE DIAGRAMS OF THE FLOW REGIMES. ESTIMATION OF THE EFFECTIVENESS OF DISPLACEMENT

By analogy with Lenormand's study [1], we have schematically illustrated the investigation results for each of the samples in the phase diagram $\log_{10}\mathrm{Ca}-\log_{10}\mathrm{M}$ (Fig. 6). The geometric symbols denote the regimes with formation of capillary fingers (diamonds), viscous fingers (circles), with conditionally stable interphase front (triangles), and the crossover zones (squares). In Fig. 6 the broken lines denote the boundaries of each type of flows and the domains inside these lines are transition domains. The investigations whose results are given in Section 2 showed that each flow regime (except for crossover regime) has a set of distinctive features which manifest themselves similarly in each of the samples and make it possible to identify the type of two-phase flow in the class of porous media of the similar type regardless of their properties. In the qualitative analysis of the diagrams it was noted that, on the one hand, the shapes of the crossover zones and, correspondingly, of the remaining flow regimes

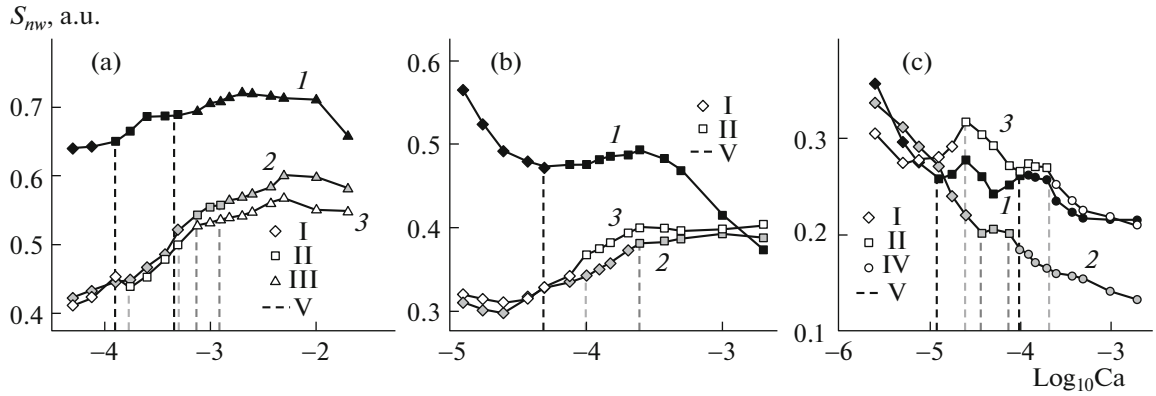

Fig. 11. Saturation of a sample with the non-wetting phase S_{nw} for various Ca at the instant of its breaking through the output cross-section for all three samples: $\log_{10} \mathrm{M} = 1, 0, -1$ (a–c), respectively); curves *1–3* correspond to the samples no. 1–3, respectively; I correspond to the capillary fingers, II to the crossover zone, III to the stable front, IV to the viscous fingers, and V show the boundaries of the flow regimes.

separated from them have similar contours, while the transition domains have different thicknesses. On the other hand, the ranges of the Ca numbers which correspond to different flow regimes shown in Fig. 6 are significantly different for each of the samples. Comparing with the filtration-capacity characteristics given in the Table 1, we can conclude that there is no correlation between them and the boundary numbers Ca. This means that for given parameters the specifics of unsteady two-phase flow depends mainly on heterogeneity of the porous space which is not determined by the integral parameters of the porous space (porosity and absolute permeability). Consequently, it is not possible to forecast the development of some flow regime for the known flow characteristics only on the basis of averaged properties of the sample without carrying out multivariant calculations.

The investigations carried out have the applied significance for estimating the effectiveness of displacement for various two-phase flow parameters. In Fig. 11 we have plotted the curves of the sample saturation by the non-wetting phase at the instant of its breaking through the output cross-section for various Ca and for each of the samples investigated, namely, for $\log_{10} \mathrm{M} = 1, 0, -1$ (Figs. 11a–11c, respectively). In these figures broken lines denote the boundaries of the flow regimes, shown also in Fig. 6. Comparing the graphs, we can conclude that growth in the viscosity of injected phase leads to increase in the saturation. When $\log_{10} \mathrm{M} = 1$ (Fig. 11a) growth in Ca leads to increase in the effectiveness of displacement in each of the samples; however, there is a small decrease in the saturation at the flow velocities 2×10^{-3} m/s and $\sigma = 2$ mN/m. When $\log_{10} \mathrm{M} = -1$ (Fig. 11c) the effectiveness of filling is significantly higher in the capillary fingering regime than that in the viscous fingering regime. In both regimes, increase in the capillary number leads to monotonic decrease in the saturation. The results which are the most problematic for interpretation are obtained when $\log_{10} \mathrm{M} = 0$ (Fig. 11b). Increase in Ca leads to decrease in the effectiveness of displacement for the sample no. 1; however, the opposite situation takes place for the sample nos. 2 and 3. Obviously, there is no correlation dependence.

Summing up the estimates of the effectiveness of displacement for all the samples, we can conclude that the saturations in each of them are different for various Ca and M. They are determined by heterogeneity of the microstructure of porous space. The stable displacement front is the most favorable regime, while the viscous fingering regime is the least favorable; it is not possible to detect the dependence of the saturation on the number Ca in the crossover regimes for any M.

In all the computational experiments the calculations were carried out till the amount of injected fluid reaches a single porous volume. In accordance with the results obtained, in the capillary fingering regime the sample contains no more than 5% of the mobile wetting liquid at the instant when injected fluid breaks through the output cross-section. In this case, from the viewpoint of the effectiveness the least favorable situation is observed at $\log_{10} \mathrm{M} = -1$ since the saturations are at the level of only 20–30%.

SUMMARY

Dynamics of two-phase flow of immiscible incompressible liquids are studied in the three-dimensional digital models of the porous space of three samples of natural sandstones over wide ranges of variation in the parameters Ca and M. The distinctive features of the capillary fingering, viscous fingering, and stable displacement front regimes are revealed. It is shown that the indications corresponding to a particular type of flow make it possible to determine its regime in the class of porous media of similar type regardless of its properties. The phase diagrams of flow regimes are constructed for each of the samples. It is found that they are determined by heterogeneities of the structure of porous space and there is no correlation with the integral (volume average) filtration-capacity properties. The quantitative estimates obtained can be used in designing full-scale experiments and for the choice of the effective displacement regimes.

The work is performed according to the Russian Government Program of Competitive Growth of Kazan Federal University and with support from the Russian Science Foundation (RSCF) under the grant no. 15-11-10015.

REFERENCES

1. R. Lenormand, E. Touboul, and C. Zarcone, "Numerical Models and Experiments on Immiscible Displacements in Porous Media," J. Fluid Mech. **189**, 165–187 (1988).
2. H. Liu, Y. Zhang, and A. J. Valocchi, "Lattice Boltzmann Simulation of Immiscible Fluid Displacement in Porous Media: Homogeneous versus Heterogeneous Pore Network," Phys. Fluids **27** (5), 052103 (2015).
3. H. Liu, A. J. Valocchi, C. Werth, Q. Kang, and M. Oostrom, "Pore-scale Simulation of Liquid CO_2 Displacement of Water Using a Two-Phase Lattice Boltzmann Model," Advances in Water Resources **73**, 144–158 (2014).
4. A. M. Tartakovsky and P. Meakin, "Pore Scale Modeling of Immiscible and Miscible Fluid Flows Using Smoothed Particle Hydrodynamics," Advances in Water Resources **29**, 1464–1478 (2006).
5. A. Ferrari and I. Lunati, "Direct Numerical Simulations of Interface Dynamics to Link Capillary Pressure and Total Surface Energy," Advances in Water Resources **57**, 19–31 (2013).
6. F. Kazemifar, G. Blois, D. C. Kyritsis, and K. Christensen, "Quantifying the Flow Dynamics of Supercritical CO_2-Water Displacement in a 2D Porous Micromodel Using Fluorescent Microscopy and Microscopic PIV," Advances in Water Resources **95**, 352–368 (2016).
7. N. A. Baryshnikov, G. V. Belyakov, and S. B. Turuntaev, "Two-Phase Jet Flows in Porous Media," Fluid Dynamics **52** (1), 128–137 (2017).
8. M. Ferer, C. Ji, G. S. Bromhal, J. Cook, G. Ahmadi, and D. H. Smith, "Crossover from Capillary Fingering to Viscous Fingering for Immiscible Unstable Flow: Experiment and Modeling," Phys. Rev. E. Statistical, Nonlinear, and Soft Matter Phys. **70**, 016303 (2004).
9. T. Tsuji, F. Jiang, and K. T. Christensen, "Characterization of Immiscible Fluid Displacement Processes with Various Capillary Numbers and Viscosity Ratios in 3D Natural Sandstone," Advances in Water Resources **95**, 3–15 (2016).
10. F. Jiang, T. Tsuji, and C. Hu, "Elucidating the Role of Interfacial Tension for Hydrological Properties of Two-Phase Flow in Natural Sandstone by an Improved Lattice Boltzmann Method," Transport in Porous Media **104**, 205–229 (2014).
11. S. Leclaire, A. Parmigiani, O. Malaspinas, B. Chopard, and J. Latt, "Generalized Three-Dimensional Lattice Boltzmann Color-Gradient Method for Immiscible Two-Phase Pore-Scale Imbibition and Drainage in Porous Media," Phys. Rev. E. **95**, 033306 (2017).
12. S. Schluter, S. Berg, M. Rucker, R. T. Armstrong, H.-J. Vogel, R. Hilfer, and D. Wildenschild, "Pore-Scale Displacement Mechanisms as a Source of Hysteresis for Two-Phase Flow in Porous Media," Water Resources Research **52**, 2194–2205 (2016).
13. S. Berg, H. Ott, S. Klapp, A. Schwing, R. Neiteler, N. Brussee, A. Makurat, L. Leu, F. Enzmann, J.-O. Schwarz, M. Kersten, S. Irvine, and M. Stampanoni, "Real-Time 3D Imaging of Haines Jumps in Porous Media Flow," Proc. National Academy of Sciences of the USA **10**, 3755–3759 (2013).
14. R. Mokso, F. Marone, D. Haberthür, J. C. Schittny, G. Mikuljan, A. Isenegger, and M. Stampanoni, "Following Dynamic Processes by X-ray Tomographic Microscopy, with Sub-Second Temporal Resolution," in: *AIP Conf. Proc., 2011*, pp. 38–41.
15. M. Mehravaran and S. K. Hannani, "Simulation of Incompressible Two-Phase Flows with Large Density Differences Employing Lattice Boltzmann and Level Set Methods," Comput. Methods Appl. Mech. Engrg. **198**, 223–233 (2008).
16. A. Q. Raeini, M. Blunt, and B. Bijeljic, "Modelling Two-Phase Flow in Porous Media at the Pore Scale Using the Volume-of-Fluid Method," J. Comput. Phys. **231**, 5653–5668 (2012).

17. V. E. Badalassi, H. D. Ceniceros, and S. Banerjee, "Computation of Multiphase Systems with Phase Field Models," J. Comput. Phys., No. 190, 371–397 (2003).
18. A. Q. Raeini, M. Blunt, and B. Bijeljic, "Direct Simulations of Two-Phase Flow on Micro-CT Images of Porous Media and Upscaling of Pore-Scale Forces," Advances in Water Resources **74**, 116–126 (2014).
19. S. Succi, *The Lattice Boltzmann Equation for Fluid Dynamics and Beyond* (Oxford Clarendon, Oxford, 2001).
20. X. Shan and H. Chen, "Lattice Boltzmann Model for Simulating Flows with Multiple Phases and Components," Phys. Rev. **3**, 1815–1819 (1993).
21. H. Huang, J.-J. Huang, and X.-Y. Lu, "Study of Immiscible Displacements in Porous Media Using a Color-Gradient-Based Multiphase Lattice Boltzmann Method," Computers & Fluids 93, 164–172 (2014).
22. I. Zacharoudiou and E. S. Boek, "Capillary Filling and Haines Jump Dynamics Using Free Energy Lattice Boltzmann Simulations," Advances in Water Resources **92**, 43–56 (2016).
23. E. Aslan, I. Taymaz, and A. C. Benim, "Investigation of the Lattice Boltzmann SRT and MRT Stability for Lid Driven Cavity Flow," Int. J. Materials, Mechanics and Manufacturing **2** (4), 317–324 (2014).
24. S. Leclaire, M. Reggio, and J.-Y. Trépanier, "Numerical Evaluation of Two Recoloring Operators for an Immiscible Two-Phase Flow Lattice Boltzmann model," Appl. Math. Modelling **36** (5), 2237–2252 (2012).
25. Q. Zou and X. He, "On Pressure and Velocity Boundary Conditions for the Lattice Boltzmann BGK Model," Phys. Fluids **9**, 1591–1598 (1997).
26. T. Reis and T. N. Phillips, "Lattice Boltzmann Model for Simulating Immiscible Two-Phase Flows," J. Phys. A: Math. Theoretical **40**, 4033–4053 (2007).
27. J. Huang, F. Xiao, and X. Yin, "Lattice Boltzmann Simulation of Pressure-Driven Two-Phase Flows in Capillary Tube and Porous Medium," Computers & Fluids 100, 164–172 (2014).
28. P. Iassonov, T. Gebrenegus, and M. Tuller, "Segmentation of X-ray Computed Tomography Images of Porous Materials: A Crucial Step for Characterization and Quantitative Analysis of Pore Structures," Water Resources Research **45** (9), 1–12 (2009).
29. P. Mostaghimi, M. J. Blunt, and B. Bijeljic, "Computations of Absolute Permeability on Micro-CT Images," Mathematical Geosciences **45**, 103–125 (2013).
30. T. R. Zakirov, A. A. Galeev, E. A. Korolev, and E. O. Statsenko, "Flow Properties of Sandstone and Carbonate Rocks by X-Ray Computed Tomography," Current Science **110** (11), 2142–2147 (2016).
31. Y. Mu, R. Sungkorn, and J. Toelke, "Identifying the Representative Flow Unit for Capillary Dominated Two-Phase Flow in Porous Media Using Morphology-Based Pore-Scale Modeling," Advances in Water Resources **95**, 16–28 (2016).
32. S. J. Jackson, H. Power, and D. Giddings, "Immiscible Thermo-Viscous Fingering in Hele-Shaw Cells," Computers and Fluids **156**, 621–641 (2017).